

Original citation:

Zhao, T., Houlsby, G. T. and Utili, Stefano. (2014) Investigation of granular batch sedimentation via DEM–CFD coupling. *Granular Matter*, 16 (6). pp. 921-932

Permanent WRAP url:

<http://wrap.warwick.ac.uk/71267>

Copyright and reuse:

The Warwick Research Archive Portal (WRAP) makes this work by researchers of the University of Warwick available open access under the following conditions. Copyright © and all moral rights to the version of the paper presented here belong to the individual author(s) and/or other copyright owners. To the extent reasonable and practicable the material made available in WRAP has been checked for eligibility before being made available.

Copies of full items can be used for personal research or study, educational, or not-for profit purposes without prior permission or charge. Provided that the authors, title and full bibliographic details are credited, a hyperlink and/or URL is given for the original metadata page and the content is not changed in any way.

Publisher's statement:

"The final publication is available at Springer via <http://dx.doi.org/10.1007/s10035-014-0534-0>

A note on versions:

The version presented here may differ from the published version or, version of record, if you wish to cite this item you are advised to consult the publisher's version. Please see the 'permanent WRAP url' above for details on accessing the published version and note that access may require a subscription.

For more information, please contact the WRAP Team at: publications@warwick.ac.uk

warwick**publications**wrap

highlight your research

<http://wrap.warwick.ac.uk>

Investigation of granular batch sedimentation via DEM-CFD coupling

T. Zhao¹, G.T. Houlsby¹, S. Utili²

¹ Department of Engineering Science, University of Oxford, Oxford, OX1 3PJ, UK

E-mail: tao.zhao@eng.ox.ac.uk

² School of Engineering, University of Warwick, Coventry CV4 7AL, UK

Abstract: This paper presents three dimensional (3D) numerical investigations of batch sedimentation of spherical particles in water, by analyses performed by the Discrete Element Method (DEM) coupled with Computational Fluid Dynamics (CFD). By employing this model, the features of both mechanical and hydraulic behaviour of the fluid-solid mixture system are captured. Firstly, the DEM-CFD model is validated by the simulation of the sedimentation of a single spherical particle, for which an analytical solution is available. The numerical model can replicate accurately the settling behaviour of particles as long as the mesh size ratio (D_{mesh}/d) and model size ratio (W/D_{mesh}) are both larger than a given threshold. During granular batch sedimentation, segregation of particles is observed at different locations in the model. Coarse grains continuously accumulate at the bottom, leaving the finer grains deposited in the upper part of the granular assembly. During this process, the excess pore water pressure initially increases rapidly to a peak value, and then dissipates gradually to zero. Meanwhile, the compressibility of the sediments decreases slowly as a soil layer builds up at the bottom. Consolidation of the deposited layer is caused by the self-weight of grains, while the compressibility of the sample decreases progressively.

Keywords: granular batch sedimentation, DEM-CFD coupling, segregation, pore water pressure, effective stress, compressibility

1 Introduction

The sedimentation and consolidation processes of granular materials are common in both terrestrial and submerged environments. In the natural environment, granular materials often settle continuously towards the seabed, lake or river floor to form a loose sediment layer. As the skeleton of the sediment layer is extremely compressible, it undergoes relatively large strain under additional loads. Sedimentation processes are very important for solid-liquid

1 separation, as can be found in the fields of chemical, mining, wastewater, food,
2 pharmaceutical and other industries [1-3]. The related research includes theoretical,
3 experimental and numerical investigations on a variety of materials [3-10].
4

5
6 During granular sedimentation, the average settling velocity of a suspension is the most
7 notable parameter quantifying the dynamic behaviour of the fluid-solid mixture system [11-
8 15]. As first proposed by Kynch [4], the average settling velocity of a suspension depends
9 only on the local concentration of solid materials (in addition to the characteristics of the
10 particles and fluid). This statement has been validated by experimental measurements of the
11 grain settling rates in granular suspension systems [6, 8, 16]. Numerical simulations of
12 sedimentation mainly focus on the settling and depositional behaviour of particles in either
13 monodisperse [7, 12, 17] or polydisperse [10, 18] systems. This research reveals three distinct
14 zones in a grain settling system, enumerated from top to bottom as: 1. the hindered settling
15 zone, where the surface settling velocity is approximately constant; 2. the transition zone
16 where the settling rate decreases gradually towards zero; and 3. the compression zone where
17 a soil layer is formed at the bottom and consolidation occurs due to the self-weight of
18 sediments. However, as reported by Richardson and Zaki [7], zone 1 is absent for very fine
19 flocculated pulps, and the settling rate decreases progressively.
20
21

22
23 For many years, analytical and numerical investigations of sedimentation employing
24 empirical correlations of the mixture properties based on laboratory experiments have been
25 reported [3, 7, 19-22]. However, a fully systematic study of sedimentation is still lacking as
26 the fluid-solid mixture presents a highly heterogeneous structure featuring a spatially non-
27 uniform distribution of particles [6, 23]. The numerical investigation reported here is based
28 on the concept that the motion of particles is completely governed by the Newtonian
29 equations of motion, and interparticle collisions are modelled by the soft particle approach [3].
30 The fluid flow is calculated by the Navier-Stokes equations [3, 11, 24]. Consequently, the
31 Discrete Element Method (DEM) [25] and Computational Fluid Dynamics (CFD) [26]
32 techniques can be used to study the mechanical and hydraulic behaviour of particles and fluid
33 flow, respectively. By coupling these two methods, a complete analysis of the sedimentation
34 of a fluid-solid mixture system can be achieved [27].
35
36

37
38 The work presented here is part of a research effort to extend the DEM modelling of
39 landslides [28-30] to the submerged case. The paper is organised as follows. We explain the
40 theory and methodology of the DEM and CFD in Section 2. The numerical investigation of
41 granular sedimentation is presented in Section 3. We first validate the DEM-CFD coupling
42
43
44
45
46
47
48
49
50
51
52
53
54
55
56
57
58
59
60
61
62
63
64
65

1 model by simulating the sedimentation of a single spherical particle (Section 3.1). Then, we
 2 analyse the batch sedimentation of particles, examining the segregation of particles,
 3 generation and dissipation of excess pore water pressures, and evolution of contact force
 4 chains (Section 3.2). Section 4 summarizes the results and main conclusions achieved by the
 5 work.
 6
 7
 8
 9

10 **2 Theory and methodology**

11 The equations governing a fluid-solid mixture system are derived from the theory of
 12 multiphase flow [27, 31]. Figure 1 illustrates the components of the mixture, which consists
 13 of fluid, and particles. The fluid density (ρ_f), velocity (\mathbf{U}) and particle packing porosity (n) are
 14 functions of spatial position and time. The DEM and CFD open source codes ESyS-Particle
 15 [32, 33] and OpenFOAM [34] were employed for the simulations presented here. The
 16 coupling algorithm from Chen *et al.* [27] originally written in YADE [35] was implemented
 17 in ESyS-Particle by the authors.
 18
 19
 20
 21
 22
 23
 24
 25
 26
 27
 28
 29

30 **2.1 Equations governing particle motion**

31 According to Newton's Second Law of motion, the equation governing the translational
 32 motion of a spherical particle is expressed as:
 33
 34
 35
 36
 37

$$38 \quad m_i \frac{d^2}{dt^2} \vec{x}_i = m_i \vec{g} + \sum_c (\vec{f}_{nc} + \vec{f}_{tc}) + \vec{f}_{fluid} \quad (1)$$

39 where m_i is the mass of particle i ; \vec{x}_i is the position of its centroid; \vec{g} is the gravitational
 40 acceleration; \vec{f}_{nc} and \vec{f}_{tc} are the normal and tangential particle-particle contact forces
 41 exerted by the neighbouring particles on particle i , which are calculated using the linear-
 42 spring and rolling resistance model as detailed by Iwashita [36], Jiang *et al.* [37] and
 43 Belheine *et al.* [38]; the summation of the contact forces is over all the particles in contact
 44 with particle i ; \vec{f}_{fluid} is the force exerted by fluid on the particle, which will be defined in
 45 Section 2.2.
 46
 47
 48
 49
 50
 51
 52
 53
 54
 55
 56

57 The rotational motion of a spherical particle is governed by Eq.(2), as:
 58
 59
 60
 61
 62
 63
 64
 65

$$I_i \frac{d}{dt} \overline{\omega}_i = \sum_c \overline{r}_c \times \overline{f}_{ic} + \overline{M}_r \quad (2)$$

where I_i is the moment of inertia about the grain centroid; $\overline{\omega}_i$ is the angular velocity; \overline{r}_c is the vector from the particle mass centre to the contact point; \overline{M}_r is the rolling resistant moment, which inhibits particle rotation over other particles. The rolling resistant moment used in the DEM model accounts approximately for the angular shape and interlocking effects between particles.

2.2 Fluid-particle interaction

The interaction force between fluid and particles (\overline{f}_{fluid}) consists of two parts: hydrostatic and hydrodynamic forces [39]. The hydrostatic force accounts for the fluid pressure gradient around an individual particle (*i.e.* buoyancy) [27, 40, 41], expressed as:

$$\overline{f}_b^i = -v_{pi} \nabla p \quad (3)$$

where \overline{f}_b^i is the hydrostatic buoyant force acting on particle i , v_{pi} is the volume of particle i ; p is the fluid pressure.

The hydrodynamic forces acting on a particle are the drag, lift and virtual mass forces. The drag force is caused by the viscous shearing effect of fluid on the particle; the lift force is caused by the high fluid velocity gradient-induced pressure difference on the surface of the particle and the virtual mass force is caused by relative acceleration between particle and fluid [42-44]. The latter two forces are normally very small when compared to the drag force in simulating fluid flow at relatively low Reynolds numbers [44]. Therefore, the lift and virtual mass forces are neglected in the current DEM-CFD coupling model. In this process, the drag force occurs when there is a non-zero relative velocity between fluid and particles. It acts at the particle centre in a direction opposite to the particle motion relative to the fluid [45]. Experimental correlations [20, 21, 46] and numerical simulations [47-49] for the drag force are reported in the literature. In this research, the drag force (F_{di}) acting on an individual particle is calculated using the empirical correlation proposed by Di Felice [22], as:

$$F_{di} = \frac{1}{2} C_d \rho_f \frac{\pi d^2}{4} |\mathbf{U} - \mathbf{V}| (\mathbf{U} - \mathbf{V}) n^{-z+1} \quad (4)$$

where C_d is the drag force coefficient; d and \mathbf{V} are particle diameter and velocity, respectively.

The porosity correction function $n^{-(\chi+1)}$ in Eq.(4) represents the influence of the packing concentration of grains on the drag force. The expression for the term χ is [22]:

$$\chi = 3.7 - 0.65 \exp \left[-\frac{(1.5 - \log_{10} \text{Re}_p)^2}{2} \right] \quad (5)$$

where $\text{Re}_p = \rho_f d n |\mathbf{U} - \mathbf{V}| / \mu$ is the Reynolds number defined at the particle size level, with μ being the fluid viscosity. In the current analyses, χ ranges from 3.4 to 3.7.

There are several definitions of drag force coefficient reported in the literature [49-51]. A comparison between these correlations and experimental data is shown in Table 1 and Figure 2. According to Figure 2, it can be observed that the correlation of Brown and Lawler [51] matches the experimental data well in the whole range of Reynolds numbers considered in this research. Therefore, the drag force coefficient is implemented in the DEM-CFD coupling model as:

$$C_d = \frac{24}{\text{Re}} (1 + 0.150 \text{Re}^{0.681}) + \frac{0.407}{1 + \frac{8710}{\text{Re}}} \quad (6)$$

The total force exerted by fluid on a single particle is therefore expressed as:

$$\overrightarrow{f}_{fluid} = -v_{pi} \nabla p + \frac{1}{2} C_d \rho_f \frac{\pi d^2}{4} |\mathbf{U} - \mathbf{V}| (\mathbf{U} - \mathbf{V}) n^{-\chi+1} \quad (7)$$

2.3 Governing equations of fluid flow

The continuity and momentum equations governing the motion of fluid flow in a fluid-solid mixture system are derived from the theory of multiphase flow [31], as:

$$\frac{\partial(\rho_f n)}{\partial t} + \nabla \cdot (\rho_f n \mathbf{U}) = 0 \quad (8)$$

$$\frac{\partial(\rho_f n \mathbf{U})}{\partial t} + \nabla \cdot (\rho_f n \mathbf{U} \mathbf{U}) = -n \nabla p + \nabla \cdot \boldsymbol{\tau} + n \rho_f \overline{\mathbf{g}} + \overline{\mathbf{f}_d} \quad (9)$$

where $\overline{f_d}$ is the average drag force per unit fluid volume, defined as $\sum_{i=1}^N F_{di} / V_{mesh}$, with N being the number of particles within the fluid mesh cell, V_{mesh} is the volume of the fluid mesh cell; τ is the fluid viscous stress tensor.

3 Numerical investigation of grain sedimentation

This research examines the settling behaviour of particles in fluid within a parallelepiped, employing the DEM coupled with CFD. The fundamental parameters governing the settling process are the fluid density (ρ_f) and viscosity (μ), the width of the parallelepiped (W), the diameter of particle (d) and the porosity of the granular packing (n). Based on the dimensional analysis performed by Richardson and Zaki [7], a function relating all these parameters is:

$$\frac{U_r}{U_0} = f\left(\frac{\rho d U_r}{\mu}, n, \frac{W}{d}\right) \quad (10)$$

where U_r is the relative settling velocity between particle and fluid, $U_0 = gd^2(\rho_s - \rho)/18\mu$ is the terminal settling velocity of a single spherical particle in fluid, calculated by Stokes' law of sedimentation [46]. In the analysis, the normalized settling time is defined as:

$$[T] = \frac{t}{t_c} = \frac{gd^2(\rho_s - \rho)t}{18\mu H} \quad (11)$$

The vertical position (h) is normalized by the initial parallelepiped height (H), as:

$$[H] = h/H \quad (12)$$

In Eq.(10), the first two dimensionless groups on the right hand side correspond to the Reynolds number and the porosity correction terms of the governing equations in the DEM-CFD coupling model (*i.e.* Eq.(4) – (6)). The size ratio (W/d) represents the influence of model size on the settling velocity of particles. As periodic boundaries are used in the lateral directions of the fluid model (see Figure 3), the influence of wall friction (non-slip effect) on the settling behaviour of particles can be neglected in the simulations.

The numerical model configuration is shown in Figure 3. The parallelepiped has cross-sectional dimensions of 0.025 m × 0.025 m and a height of 1.0 m. The particles of various sizes are initially randomly generated within the parallelepiped and then settle downwards under gravity. The input parameters of the simulations are listed in Table 2.

3.1 Sedimentation of a single particle

A simulation of the sedimentation of a single particle has been used to validate the DEM-CFD coupling code. A spherical particle with radius 1 mm settles from a position 9 cm below the upper surface of the fluid model. The porosity of the fluid mesh cell in which the particle is placed is calculated as 0.99. The motion of the spherical particle is governed by:

$$\frac{4}{3}\pi r^3 \rho_s \frac{\partial U_r}{\partial t} = \frac{4}{3}\pi r^3 (\rho_s - \rho_f) g - \frac{1}{2}\pi r^2 \rho_f C_d U_r^2 \quad (13)$$

where $r = d/2$ is the particle radius.

In Eq.(13), the drag force coefficient (C_d) is calculated from Eq.(6). Since U also appears in the expression of the drag coefficient, it is not straightforward to obtain a solution for the settling velocity from Eq.(13) explicitly. Thus, a forward finite difference numerical technique is used to calculate the relative settling velocity at different times.

In Figure 4, the calculated analytical results for settling velocity are compared with the numerical ones. In this test, the fluid domain is meshed in the x -, y - and z -directions with $5 \times 5 \times 200$ equal sized parallelepiped cells. The particle settles from an initial static state and then accelerates until the terminal velocity is reached. The numerical results match analytical ones calculated by Eq.(13) well. The terminal velocity of the particle is 0.28 m/s.

As the coupling methodology only describes the average parameters (*e.g.* drag force, flow velocity, pressure) of the fluid-solid mixture, the fluid flow around the particles is not explicitly represented. During the calculation, the local porosity is assumed to be evenly distributed within one fluid mesh element [52]. In order to get accurate results, several DEM particles are required to fit inside one CFD mesh element, which means that the size ratio between fluid mesh dimension (D_{mesh}) and particle diameter (d) should be larger than some critical values. A series of numerical simulations with different mesh size ratios were conducted to explore this size effect: the size of fluid mesh was varied from 0.0025 m to 0.025 m, while the particle diameter was held constant for different simulations). The

1 terminal velocity of grains is normalized by the analytical settling velocity of a single particle
2 (U_0), as shown in Figure 5.
3

4 The value of mesh size ratio (D_{mesh}/d) reflects the accuracy of the averaging process
5 used in the DEM-CFD coupling model. If it is too small, fluctuation of settling velocity
6 occurs across the domain due to the heterogeneous packing of the fluid-solid mixture.
7 According to Figure 5, the particle settling velocity matches the theoretical value when the
8 size ratio (D_{mesh}/d) is larger than 5. This conclusion agrees well with the critical mesh-grain
9 size ratio suggested by Itasca [52] for the settling behaviour of a single particle.
10

11 In general, to consider the resolution of CFD calculation and possible boundary wall
12 friction effects, one needs to study the influence of the model size ratio (*i.e.* the ratio between
13 the width of the fluid model (W) and the mesh size (D_{mesh})) on the granular settling behaviour.
14 Itasca [52] suggest that this ratio should be no less than 5 and that the implementation of
15 periodic boundaries in the CFD can effectively reduce the boundary wall friction effects. The
16 Itasca recommendations are implemented in the current model, and the numerical results
17 obtained are therefore thought to be independent of the boundary wall friction effects.
18
19
20
21
22
23
24
25
26
27
28
29
30
31

32 **3.2 Numerical simulation of batch granular sedimentation**

33 For numerical simulations of granular batch sedimentation, 6000 polydispersed particles
34 are randomly generated within a parallelepiped (see Figure 3). The particle size distribution
35 (PSD) is checked along the parallelepiped. As shown in Figure 6, the PSD curves at three
36 locations along the parallelepiped (base, middle and top) overlap each other, indicating that
37 the initial DEM sample is uniform. The average porosity is 0.89. In the following analyses,
38 the fluid model is meshed in x -, y - and z -directions with $5 \times 5 \times 200$ equal sized fixed-grid
39 parallelepiped cells, as above.
40
41
42
43
44
45
46
47
48
49

50 **3.3 Observations from numerical analysis**

51 **3.3.1. Segregation of particles**

52 According to Stokes' law of sedimentation [46], during the settling process, coarse grains
53 settle faster than the finer ones, leading to segregation of grains. To illustrate this, we present
54
55
56
57
58
59
60
61
62
63
64
65

1 the particle size distribution at different locations in the sample in Figure 7. The system has
 2 been divided into three layers (base, middle and top), with each layer containing the same
 3 amount of particles. At the beginning of sedimentation, segregation is not significant, with
 4 the three PSD curves almost the same as those of the initial assembly. At $[T] = 1.8$, the PSD
 5 curve of the base region deviates slightly below the initial PSD due to the accumulation of
 6 coarse grains at the bottom. As the simulation continues, the PSD curves of the upper and
 7 bottom regions deviate gradually from the initial PSD curve. The PSD curve for the middle
 8 region remains almost the same as the initial PSD curve until $[T] = 3.6$, and then deviates
 9 gradually towards the PSD curve of grains in the base region. These observations indicate
 10 that the coarse grains move faster than the finer ones, leading to a higher concentration of
 11 coarse grains at the base and finer grains at the top.
 12
 13
 14
 15
 16
 17
 18
 19
 20

21 Initially, coarse grains in the top layer settle into the middle layer, while the coarse grains
 22 in the middle layer settle into the base layer. As a result, only the portion of coarse grains at
 23 the top and base layers have changed, while the PSD in the middle layer remains unchanged.
 24 After $[T] = 5.4$, a relatively thick deposit is formed at the base, and the PSD curves of the
 25 three layers remain unchanged. Even though some fine grains are still suspended in the fluid,
 26 they settle very slowly on top of the deposit. At the end of the simulation, only the PSD curve
 27 for the upper region lies above the initial PSD curve, while the PSD curves of grains in the
 28 middle and base layers overlap each other and lie slightly below the initial PSD curve. This
 29 indicates that in small scale sedimentation simulations, the segregation of grains manifests
 30 itself principally as a higher concentration of fine grains at the top of the sediment layer.
 31
 32
 33
 34
 35
 36
 37
 38
 39
 40

41 **3.3.2. Density profile**

42 An important feature of batch sedimentation is the gradual change of bulk density of the
 43 suspension due to the segregation of particles. The bulk density can be calculated as:
 44
 45
 46
 47

$$48 \rho_b = n\rho_f + (1-n)\rho_s \quad (14)$$

49 where ρ_b is the bulk density ρ_s is the density of solid materials.
 50
 51
 52
 53
 54

55 During the simulation, the porosity in each fluid cell is recorded, which is used to
 56 calculate the bulk density, Eq.(14). Figure 8 illustrates the evolution of the bulk density
 57 profiles of the fluid-solid mixture. It can be observed that the bulk density of the suspension
 58
 59
 60
 61
 62
 63
 64
 65

1
2
3
4
5
6
7
8
9
10
11
12
13
14
15
16
17
18
19
20
21
22
23
24
25
26
27
28
29
30
31
32
33
34
35
36
37
38
39
40
41
42
43
44
45
46
47
48
49
50
51
52
53
54
55
56
57
58
59
60
61
62
63
64
65

increases gradually along the parallelepiped height towards the bottom due to the segregation of grains. In the bottom region, grains accumulate to form a dense sediment layer, which consolidate progressively under the self-weight of the overlying grains. After $[T] = 10.8$, the bulk density at the bottom reaches an approximately constant value of 1965 kg/m^3 . A video of the simulation showing the particles settling in 3D is provided in the supplementary material.

It is possible to extract the positions of grains during the DEM simulation. Figure 9 illustrates the granular column at four settling times, in which a grid is superimposed on the sample to show the relative location of the grains. To visualize the grain motion, particles at different heights of the parallelepiped are coloured red and green. By tracking the positions of the uppermost grains, the position of the fluid–suspension interface is obtained. However, as many grains decelerate and consolidate at the bottom, there is no well-defined interface between suspension and sediment. Thus, a close comparison between several successive snapshots of the model is carried out to find a stable position of the suspension-sediment interface at a specific time. The evolution of the suspension-sediment interface is plotted as a dashed curve in Figure 10.

Based on Figure 8, a series of constant density points along the parallelepiped at different settling times was mapped onto Figure 10. In this figure it can be observed that the general patterns of constant density curves is similar to the theoretical results of sedimentation by Kynch [4]. More specifically, the upper surface initially accelerates downwards to reach a constant velocity within a very short time and then settles at a constant velocity towards the bottom. As the initial suspension is uniformly generated, the height against time curve is a straight line in the hindered settling zone. When the sediments approach the bottom, they decelerate due to grain interactions until the settling velocities become zero. In the suspension, the bulk density ranges from 1000 to 1500 kg/m^3 . The observations obtained in this research match the analytical results by Tiller [5] well.

As the grains accumulate at the bottom, the bulk density changes gradually from the intermediate to dense packing state, as represented by the density change between the suspension, zones of intermediate density and the top of relatively dense grain layers. In addition, the stable suspension-sediment interface curve passes through the intermediate density region and is very close to the 1700 kg/m^3 density curve, which suggests that a stable soil structure can be formed with density being equal to or larger than 1700 kg/m^3 .

3.3.3. Excess pore water pressure and effective stress

During the simulation, the excess pore water pressure (u) along the parallelepiped is recorded in the CFD model, based on which, the evolution of the excess pore water pressure at the bottom of the parallelepiped is obtained (see Figure 11). In Figure 11, the measured excess pore water pressures are normalized by the hydrostatic pressure of water at the bottom of the parallelepiped ($p_0 = \rho_f gH$). As the particles accelerate immediately after the application of gravity, the normalized excess pore water pressure increases quickly to reach the peak value of 0.17 at $[T] = 0.54$. After that time, a loose soil structure builds up at the bottom, and the excess pore water pressure dissipates gradually. In this process, a linear dissipation period is observed between $[T] = 0.54$ and $[T] = 7.2$. After $[T] = 7.2$, a stable sediment layer is formed at the bottom region, and the excess pore water pressure dissipates slowly due to consolidation of the sediment.

Considering the fact that some particles accumulate at the bottom of the parallelepiped before $[T] = 0.54$ in Figure 11, the measured value of maximum normalised excess pore water pressure should be smaller than the analytical value. A rational estimation of the peak normalised excess pore water pressure in Figure 11 can be the intercept of the linear pressure line on the vertical axis at point A, with a normalized excess pore water pressure of 0.178. On the other hand, the analytical maximum normalised excess pore water pressure can be calculated as the difference between total stress and the hydrostatic water pressure of the system at the beginning of the simulation (see Eq.(15)).

$$u_{e_max}/p_0 = \frac{[n\rho_f + (1-n)\rho_s]gH - \rho_f gH}{\rho_f gH} = (1-n) \left(\frac{\rho_s}{\rho_f} - 1 \right) \quad (15)$$

Based on the input parameters, the analytical maximum normalised excess pore water pressure of the fluid-solid mixture system is calculated as 0.18 which can match the estimated peak value from Figure 11 (≈ 0.178) very well.

The isochrones of excess pore water pressure at different times are illustrated in Figure 12(a). As only water exists in the region above the water-suspension interface, the excess pore water pressure remains nil in that region. From $[T] = 0.54$, the excess pore water pressure builds up and varies linearly along the parallelepiped. As time passes, a linear distribution of excess pore water pressure remains in the upper part of the parallelepiped, while at the bottom, there is a region of constant excess pore water pressure. This can be

1 explained by the fact that, once the grains stop moving, there is no relative motion between
 2 particles and fluid, and therefore no excess pore water pressure gradient exists in the
 3 sediment. However, in the suspension, the particles can settle downwards continuously, and
 4 thus, the linear distribution pattern remains unaltered there. A qualitative comparison can be
 5 made between the numerical results of our study (Figure 12(a)) and the experimental results
 6 from Been and Sills [8] (Figure 12 (b)). Even though the materials used in the numerical and
 7 experimental models are quite different, the general features of the isochrones of excess pore
 8 water pressure presented as dimensionless parameters are qualitatively the same.
 9
 10
 11
 12
 13
 14

15 During the simulation, the total stress acting on the bottom of the parallelepiped is
 16 calculated from the pore water pressure and contact forces, as:
 17
 18

$$19 \quad \sigma = p_s + u + \frac{F}{S} \quad (16)$$

20 where p_s is the hydrostatic pressure; u is the excess pore water pressure; F is the contact force
 21 exerted by grains on the bottom of the parallelepiped; S is the cross section area of the
 22 parallelepiped.
 23
 24
 25
 26
 27
 28
 29

30 Figure 13 shows that the total stress measured at the bottom of the parallelepiped is
 31 almost constant throughout the simulation. The constant total stress indicates that the periodic
 32 boundary condition employed in the simulation have effectively reduced the influence of wall
 33 friction on the overall settling behaviour of particles.
 34
 35
 36
 37

38 According to Been [16], the total stress of the suspension along the parallelepiped can be
 39 evaluated by integrating the density profiles, while the effective stress is calculated by
 40 subtracting the measured pore water pressure from the total stress. Figure 14 illustrates the
 41 distribution of pore water pressure and total stress along the parallelepiped at $[T] = 3.6$. At
 42 this time, the particles initially located in the upper region of the parallelepiped (above point
 43 A) have already settled, such that only water exists there. Thus, the pore water pressure is
 44 equal to the total stress. In the suspension (between the points A and B), grains can either
 45 settle at a constant velocity (near Point A) or collide with each other, forming a loose soil
 46 structure (near Point B). The weight of particles is partly or wholly supported by the fluid
 47 viscous drag and hydrostatic forces. Thus, the profile of pore water pressure deviates
 48 gradually from the total stress curve, indicating that effective stress occurs within the sample.
 49
 50
 51
 52
 53
 54
 55
 56
 57
 58
 59
 60
 61
 62
 63
 64
 65

1
2 In the sediment zone (below point B), the dense soil structure can sustain the overlying loads
3 and a relatively large effective stress occurs there.

4 The relationship between void ratio and normalized effective stress (σ') within the soil
5 sample at different settling times is shown in Figure 15. In this figure, three distinct zones can
6 be identified: settling, transition and consolidation zones. The settling zone appears when the
7 normalized effective stress is smaller than 0.01. In this zone, the void ratio varies widely from
8 4.0 to 14, indicating that the soil is extremely compressible. In the transition zone, a loose soil
9 structure begins to build up and the normalised effective stress increases from 0.01 to 0.05,
10 while the void ratio decreases from 5.0 to 0.5 gradually. However, no unique relationship
11 between void ratio and effective stress is observed, which is close to the observation reported
12 in Been and Sills [8]. In the consolidation zone, the compressibility of soil is low and the void
13 ratio varies very little.
14
15
16
17
18
19
20
21
22
23

24 **3.3.4. Force chains**

25
26 During the sedimentation, the sediments accumulate gradually at the bottom of the
27 parallelepiped to form a structured soil layer, which can be visualized by plotting the contact
28 force chains of the whole granular assembly. Straight lines are used to connect the centres of
29 each pair of particles in contact. The width of these lines is proportional to the magnitude of
30 contact forces, while the orientation aligns with the contact force vectors. By plotting all the
31 contact forces as straight lines, a graph of force chains of the sample can be obtained.
32
33
34
35
36
37
38

39 As shown in Figure 16, the contact force is normalized by the characteristic hydrostatic
40 force acting on the cross section of a particle (*e.g.* the diameter is D) at the bottom of the
41 parallelepiped:
42
43
44
45

$$46 [F] = \frac{F}{(\rho_s - \rho_f)gH_l D^2} \quad (17)$$

47
48
49 At the beginning of the simulation, the sediment layer is very thin, so that the contact
50 forces between grains are small. As the soil structure builds up, the magnitude of contact
51 force is mainly controlled by the self-weight of particles. Due to consolidation, the contact
52 forces at the bottom region of the model increase gradually. The strong force chains of the
53 final stable soil structure preferably orient vertically, indicating that the self-weight of soil
54 has a significant influence on the distribution of contact forces.
55
56
57
58
59
60
61
62
63
64
65

4 Conclusions

This paper sets out to investigate granular sedimentation via DEM-CFD coupled simulations. A benchmark simulation of the sedimentation of a single spherical particle in fluid was used to validate the numerical model. In this test, the settling velocity matches the available analytical solutions well. Criteria for assessing the accuracy of the DEM-CFD coupling calculations are provided, *i.e.* the size ratio between fluid mesh size and particle diameter should be larger than 5. It is also shown that the use of periodic boundaries in the lateral directions of the fluid model can effectively reduce the fluid boundary wall friction effects.

During batch sedimentation, progressive segregation of particles can be visualized by curves of the particle size distribution at different locations. Segregation is significant near the upper region of the model, while it is not so evident in the middle and bottom regions. In this process, the coarse grains accumulate at the bottom, leaving the finer ones to settle onto the surface of the deposit. As a result, the bulk density of the fluid-solid mixture decreases gradually with the height. At the end of the simulation, the bulk density of sediments is a constant value (*i.e.* 1965 kg/m³). The curves describing the vertical downward trajectory of the fluid–suspension interface and the increase of suspension–sediment interface are in agreement with the theoretical results proposed by Kynch [4].

As particles continuously settle downwards, forming a loose layer at the bottom of the parallelepiped domain, sediments consolidate slowly under the weight of the overlying grains. During this process, excess pore water pressure builds up then dissipates slowly. The normalized maximum excess pore water pressure of the suspension is 0.178, which is very close to the analytical value. The isochrones of the excess pore water pressure exhibit a qualitative agreement with the experimental results by Been and Sills [8].

In this paper, a DEM-CFD coupling formulation is presented for the investigation of grain sedimentation in fluids. Many other applications of the formulation are possible, *e.g.* submarine landslides, mudflows and river scouring. The computational efficiency of the numerical model depends highly on the numbers of particles present and the size of the mesh cells in the CFD model.

Acknowledgments

This work of the first author is supported by Marie Curie Actions-International Research Staff Exchange Scheme (IRSES). "geohazards and geomechanics", Grant No. 294976.

1
2
3
4
5
6
7
8
9
10
11
12
13
14
15
16
17
18
19
20
21
22
23
24
25
26
27
28
29
30
31
32
33
34
35
36
37
38
39
40
41
42
43
44
45
46
47
48
49
50
51
52
53
54
55
56
57
58
59
60
61
62
63
64
65

References

1. Bürger, R. and Wendland, W. L. (2001), Sedimentation and suspension flows: Historical perspective and some recent developments, *Journal of Engineering Mathematics*, 41 (2), 101-116.
2. Di Felice, R. (1999), The sedimentation velocity of dilute suspensions of nearly monosized spheres, *International Journal of Multiphase Flow*, 25 (4), 559-574.
3. Komiwies, V., Mege, P., Meimon, Y., and Herrmann, H. (2006), Simulation of granular flow in a fluid applied to sedimentation, *Granular Matter*, 8 (1), 41-54.
4. Kynch, G. J. (1952), A theory of sedimentation, *Transactions of the Faraday Society*, 48, 166-176.
5. Tiller, F. M. (1981), Revision of kynch sedimentation theory, *AIChE Journal*, 27 (5), 823-829.
6. Font, R. (1988), Compression zone effect in batch sedimentation, *AIChE Journal*, 34 (2), 229-238.
7. Richardson, J. F. and Zaki, W. N. (1954), Sedimentation and fluidisation: Part I, *Chemical Engineering Research and Design*, 75, Supplement (0), S82-S100.
8. Been, K. and Sills, G. C. (1981), Self-weight consolidation of soft soils: an experimental and theoretical study, *Géotechnique*, 31 (4), 519-535.
9. Tsuji, Y., Kawaguchi, T., and Tanaka, T. (1993), Discrete particle simulation of two-dimensional fluidized bed, *Powder Technology*, 77 (1), 79-87.
10. Shih, Y. T., Gidaspow, D., and Wasan, D. T. (1987), Hydrodynamics of sedimentation of multisized particles, *Powder Technology*, 50 (3), 201-215.
11. Wachmann, B., Kalthoff, W., Schwarzer, S., and Herrmann, H. J. (1998), Collective drag and sedimentation: comparison of simulation and experiment in two and three dimensions, *Granular Matter*, 1 (2), 75-82.
12. Batchelor, G. K. and Green, J. T. (1972), The hydrodynamic interaction of two small freely-moving spheres in a linear flow field, *Journal of Fluid Mechanics*, 56, 375-400.
13. Hinch, E. J. (1977), An averaged-equation approach to particle interactions in a fluid suspension, *Journal of Fluid Mechanics*, 83, 695-720.
14. Batchelor, G. K. (1982), Sedimentation in a dilute polydisperse system of interacting spheres. Part 1. General theory, *Journal of Fluid Mechanics*, 119, 379-408.
15. Batchelor, G. K. and Wen, C. S. (1982), Sedimentation in a dilute polydisperse system of interacting spheres. Part 2. Numerical results, *Journal of Fluid Mechanics*, 124, 495-528.
16. Been, K. (1980), Stress strain behaviour of a cohesive soil deposited under water, (University of Oxford), 257.
17. Mills, P. and Snabre, P. (1994), Settling of a Suspension of Hard Spheres, *EPL (Europhysics Letters)*, 25 (9), 651.
18. Davis, R. H. and Gecol, H. (1994), Hindered settling function with no empirical parameters for polydisperse suspensions, *AIChE Journal*, 40 (3), 570-575.
19. Othmer, D. F. (1956), *Fluidization* (New York: Reinhold Publishing Corporation), 231.
20. Ergun, S. (1952), Fluid flow through packed columns, *Chemical Engineering Progress*, 48 (2), 89-94.
21. Wen, C. Y. and Yu, Y. H. (1966), Mechanics of fluidization, *Chemical Engineering Progress Symposium Series*, 62 (62), 100-111.
22. Di Felice, R. (1994), The voidage function for fluid-particle interaction systems, *International Journal of Multiphase Flow*, 20 (1), 153-159.
23. Fitch, B. (1983), Kynch theory and compression zones, *AIChE Journal*, 29 (6), 940-947.
24. Kalthoff, W., Schwarzer, S., Ristow, G., and Herrmann, H. J. (1996), On the application of a novel algorithm to hydrodynamic diffusion and velocity fluctuations in sedimenting systems, *International Journal of Modern Physics C*, 07 (04), 543-561.
25. Cundall, P. A. and Strack, O. D. L. (1979), A discrete numerical model for granular assemblies, *Géotechnique*, 29 (1), 47-65.
26. Anderson, J. D. (1995), *Computational fluid dynamics: the basics with applications* (McGraw-Hill), 547.

27. Chen, F., Drumm, E. C., and Guiochon, G. (2011), Coupled discrete element and finite volume solution of two classical soil mechanics problems, *Computers and Geotechnics*, 38 (5), 638-647.
28. Utili, S. and Crosta, G. B. (2011), Modeling the evolution of natural cliffs subject to weathering: 1. Limit analysis approach, *Journal of Geophysical Research: Earth Surface*, 116 (F1), F01016.
29. Boon, C. W., Houlsby, G. T., and Utili, S. (2014), New insights in the 1963 Vajont slide using 2D and 3D Distinct Element Method analyses, *Geotechnique*, in press.
30. Utili, S. and Crosta, G. B. (2011), Modeling the evolution of natural cliffs subject to weathering: 2. Discrete element approach, *Journal of Geophysical Research: Earth Surface*, 116 (F1), F01017.
31. Brennen, C. E. (2005), *Fundamentals of Multiphase Flow* (Cambridge University Press), 368.
32. Weatherley, D., Boros, V., and Hancock, W. (2011), *ESyS-Particle Tutorial and User's Guide Version 2.1* (Earth Systems Science Computational Centre, The University of Queensland), 153.
33. Abe, S., Place, D., and Mora, P. (2004), A Parallel Implementation of the Lattice Solid Model for the Simulation of Rock Mechanics and Earthquake Dynamics, *pure and applied geophysics*, 161 (11-12), 2265-2277.
34. OpenCFD OpenFOAM - The open source CFD toolbox, <http://www.openfoam.com/>.
35. V. Šmilauer, E. Catalano, B. Chareyre, S. Dorofeenko, J. Duriez, A. Gladky, J. Kozicki, C. Modenese, L. Scholtès, L. Sibille, J. Stránský, K. Thoeni (2010), Yade Documentation, (The YADE Project; <http://yade-dem.org/doc/>).
36. Iwashita, K. (1998), Rolling resistance at contacts in simulation of shear band development by DEM, *Journal of Engineering Mechanics*, 124 (285), 285-292.
37. Jiang, M. J., Yu, H. S., and Harris, D. (2005), A novel discrete model for granular material incorporating rolling resistance, *Computers and Geotechnics*, 32 (5), 340-357.
38. Belheine, N., Plassiard, J. P., Donzé, F. V., Darve, F., and Seridi, A. (2009), Numerical simulation of drained triaxial test using 3D discrete element modeling, *Computers and Geotechnics*, 36 (1-2), 320-331.
39. Shafipour, R. and Soroush, A. (2008), Fluid coupled-DEM modelling of undrained behavior of granular media, *Computers and Geotechnics*, 35 (5), 673-685.
40. Kafui, D. K., Johnson, S., Thornton, C., and Seville, J. P. K. (2011), Parallelization of a Lagrangian-Eulerian DEM/CFD code for application to fluidized beds, *Powder Technology*, 207 (1-3), 270-278.
41. Zeghal, M. and El Shamy, U. (2004), A continuum-discrete hydromechanical analysis of granular deposit liquefaction, *International Journal for Numerical and Analytical Methods in Geomechanics*, 28 (14), 1361-1383.
42. Drew, D. A. and Lahey, R. T. (1990), Some supplemental analysis concerning the virtual mass and lift force on a sphere in a rotating and straining flow, *International Journal of Multiphase Flow* 16 (6), 1127-1130.
43. DEMSolutions (2010), *EDEM-CFD Coupling for FLUENT: User Guide*, 25.
44. Kafui, K. D., Thornton, C., and Adams, M. J. (2002), Discrete particle-continuum fluid modelling of gas-solid fluidised beds, *Chemical Engineering Science*, 57 (13), 2395-2410.
45. Guo, Yu (2010), A coupled DEM/CFD analysis of die filling process - PhD Thesis, (The University of Birmingham), 309.
46. Stokes, G. G. (1901), *Mathematical and physical papers* (Cambridge University Press), 416.
47. Choi, H. G. and Joseph, D. D. (2001), Fluidization by lift of 300 circular particles in plane Poiseuille flow by direct numerical simulation, *Journal of Fluid Mechanics*, 438, 101-128
48. Zhang, J., Fan, L. S., Zhu, C., Pfeffer, R., and Qi, D. (1999), Dynamic behavior of collision of elastic spheres in viscous fluids, *Powder Technology*, 106 (1-2), 98-109.
49. Beetstra, R., van der Hoef, M. A., and Kuipers, J. A. M. (2007), Drag force of intermediate Reynolds number flow past mono- and bidisperse arrays of spheres, *AIChE Journal*, 53 (2), 489-501.
50. DallaValle, J. M. (1948), *Micromeritics : The Technology of Fine Particles* (Pitman Pub. Corp; 2nd edition), 555.

51. Brown, P. and Lawler, D. (2003), Sphere Drag and Settling Velocity Revisited, *Journal of Environmental Engineering*, 129 (3), 222-231.
52. Itasca (2008), *CCFD-PFC documentaton*, 1.0 vols. (Minnesota, USA: Itasca Consulting Group Inc), 104.

1
2
3
4
5
6
7
8
9
10
11
12
13
14
15
16
17
18
19
20
21
22
23
24
25
26
27
28
29
30
31
32
33
34
35
36
37
38
39
40
41
42
43
44
45
46
47
48
49
50
51
52
53
54
55
56
57
58
59
60
61
62
63
64
65

1
2
3 Figure 1. An infinitesimally small element of the fluid-solid system
4
5
6

7
8 Figure 2. Drag coefficient of various correlations and experimental data for spherical particles
9
10

11
12
13 Figure 3. Configuration of the granular sedimentation model
14
15
16

17
18 Figure 4. The fluid settling velocity for a particle with diameter being 1 mm
19
20
21

22
23
24 Figure 5. The effect of size ratio (D_{mesh}/d) on the normalized settling velocity
25
26
27

28
29 Figure 6. The particle size distribution curve of the sample at three different locations
30
31
32

33
34 Figure 7. Particle size distributions in suspensions and sediments at different times.
35
36
37

38
39 Figure 8. The density profile of the fluid-solid mixture at different normalized times
40
41
42

43 Figure 9. Measurement of sediments height
44
45
46

47 Figure 10. Height against time plot for constant density curves
48
49
50

51
52 Figure 11. Evolution of pore pressure at the bottom of parallelepiped (p_0 is the hydrostatic
53 pressure)
54
55
56

57
58 (a) The DEM-CFD simulation results
59
60
61
62
63
64
65

(b) Results from Been [8] (the time has been normalized by the characteristic settling time of a grain with diameter being 5 μm)

Figure 12. Isochrones of excess pore water pressure along the parallelepiped at different times

Figure 13. Total stress at the base of the bottom

Figure 14. Stress distribution along the parallelepiped at $[T] = 3.6$

Figure 15. The void ratio against normalized effective stress at various simulation time

Figure 16. Force chain of the sediments at different times

Table 1. Some correlations of drag force coefficient for spherical particles

Table 2. Input parameters of the sedimentation simulation

Figure

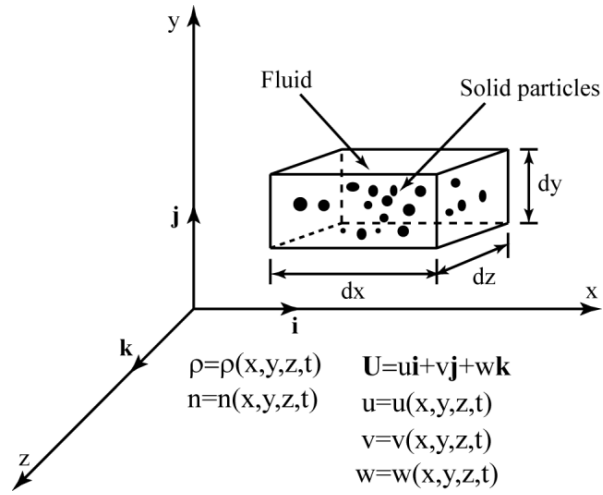


Figure 1. An infinitesimally small element of the fluid-solid system

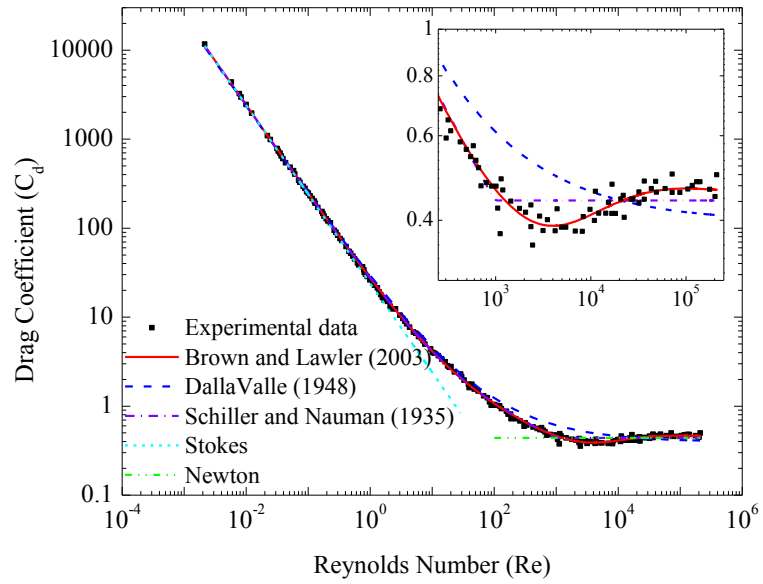


Figure 2. Drag coefficient of various correlations and experimental data for spherical particles

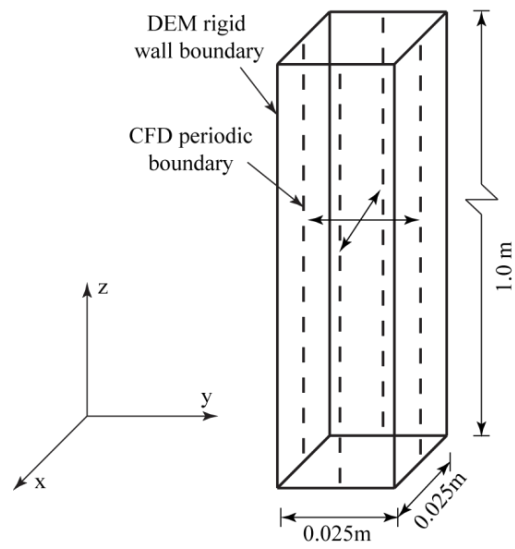


Figure 3. Configuration of the granular sedimentation model

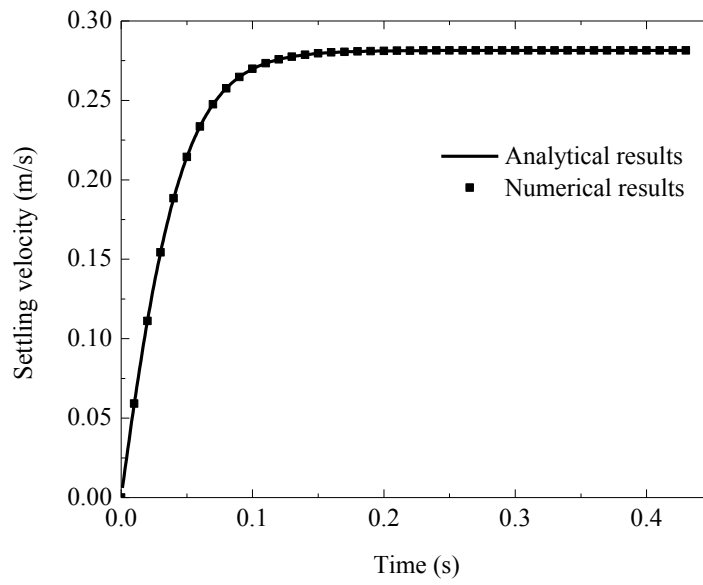


Figure 4. The settling velocity of a single spherical particle ($D = 1$ mm)

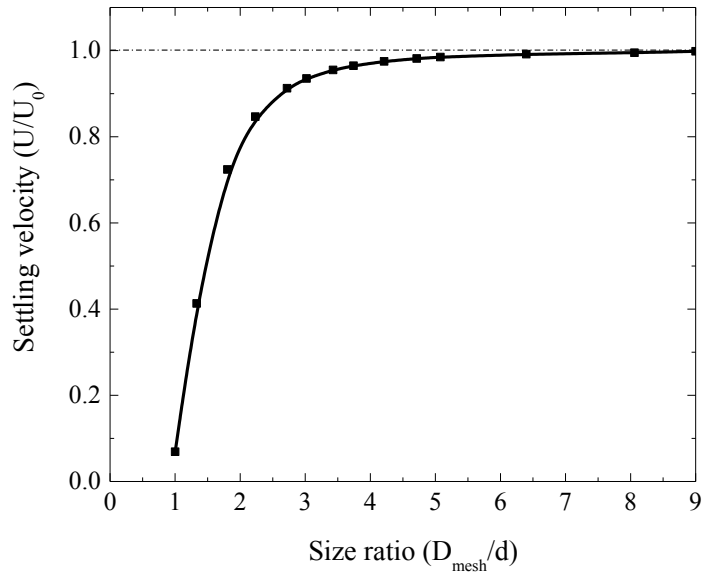


Figure 5. The effect of size ratio (D_{mesh}/d) on the normalized settling velocity

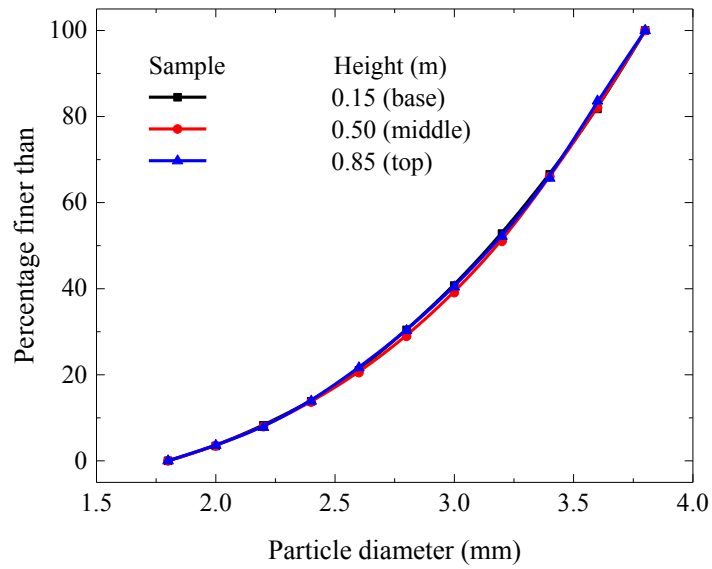


Figure 6. The particle size distribution curve of the sample at three different locations

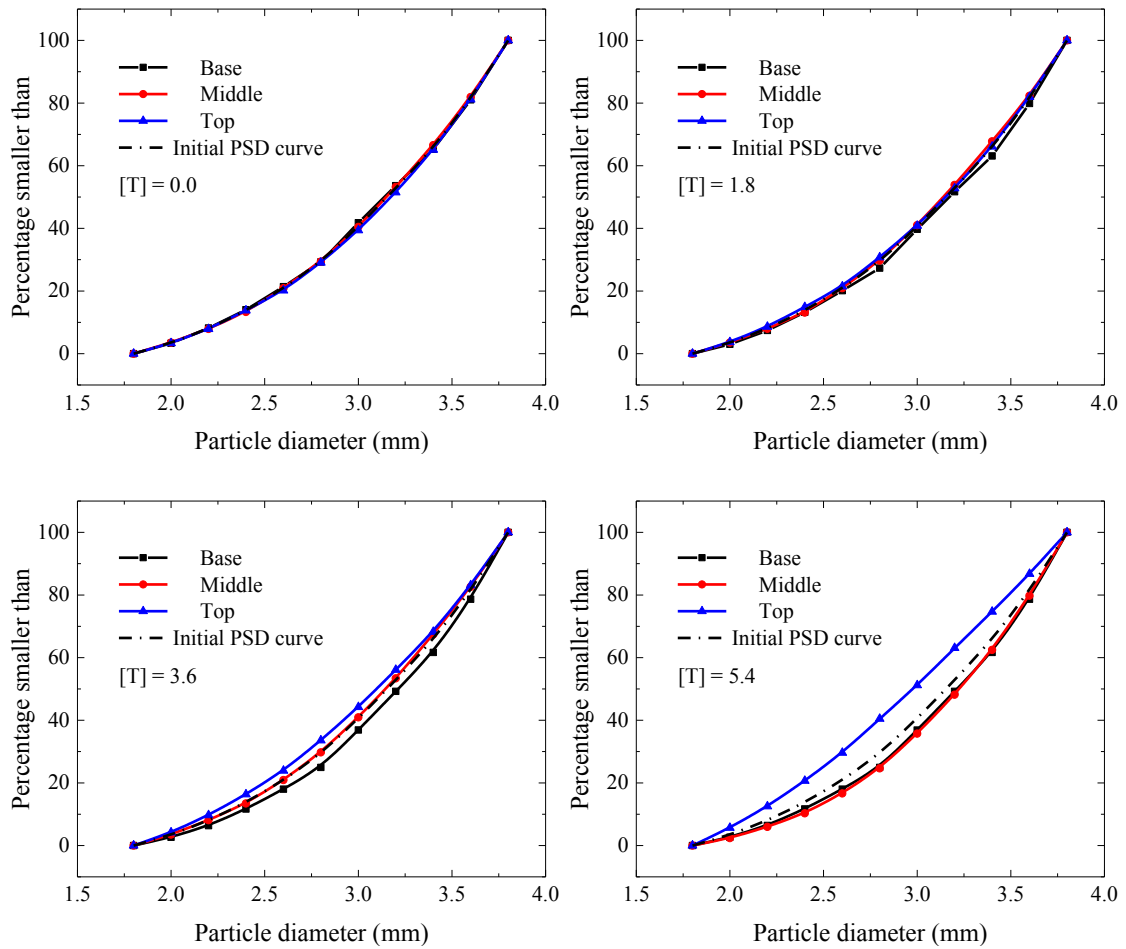


Figure 7. Particle size distribution in suspensions and sediments at different times.

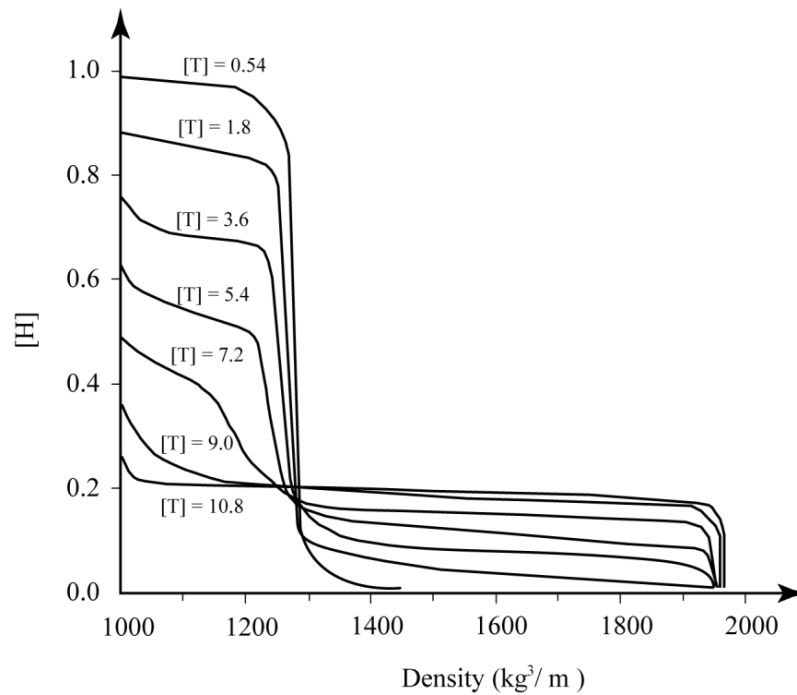


Figure 8. Density profiles of the fluid-solid mixture at different normalized times

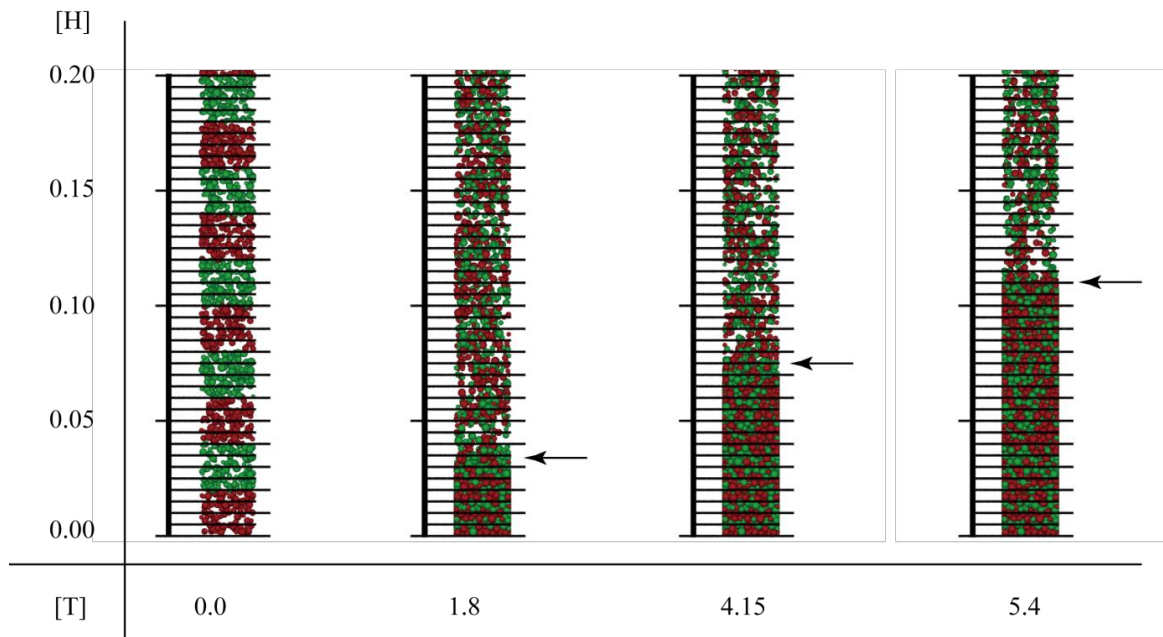


Figure 9. Measurement of sediments height

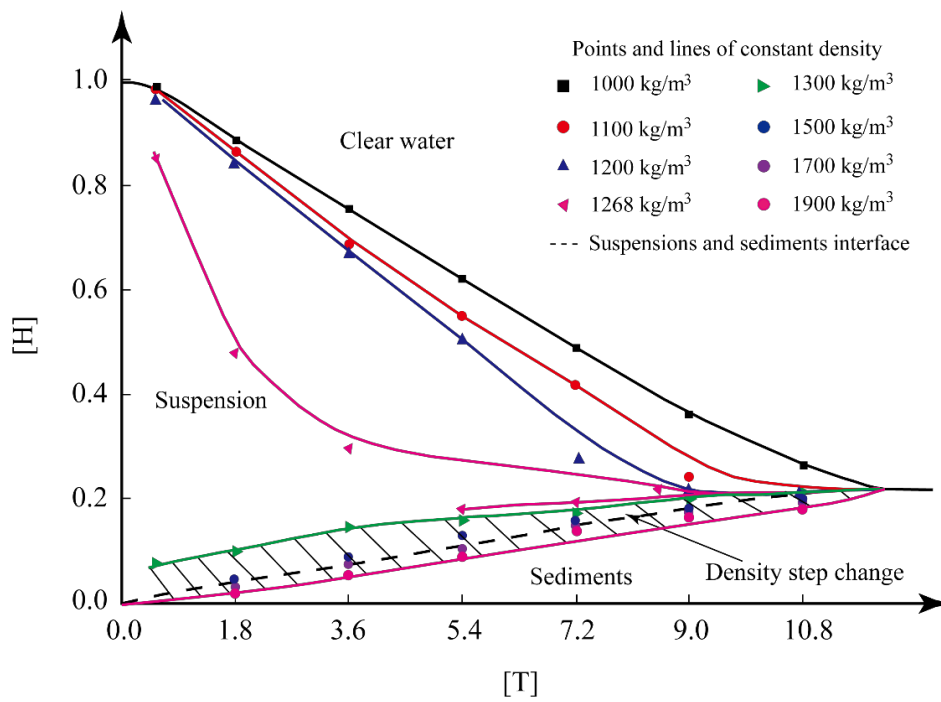


Figure 10. Height against time plot for constant density curves

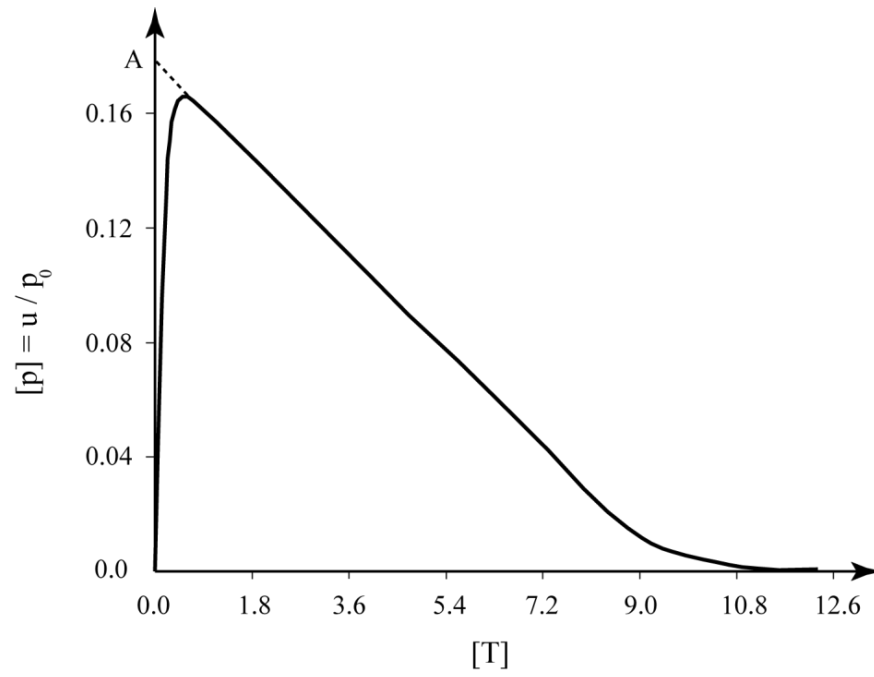
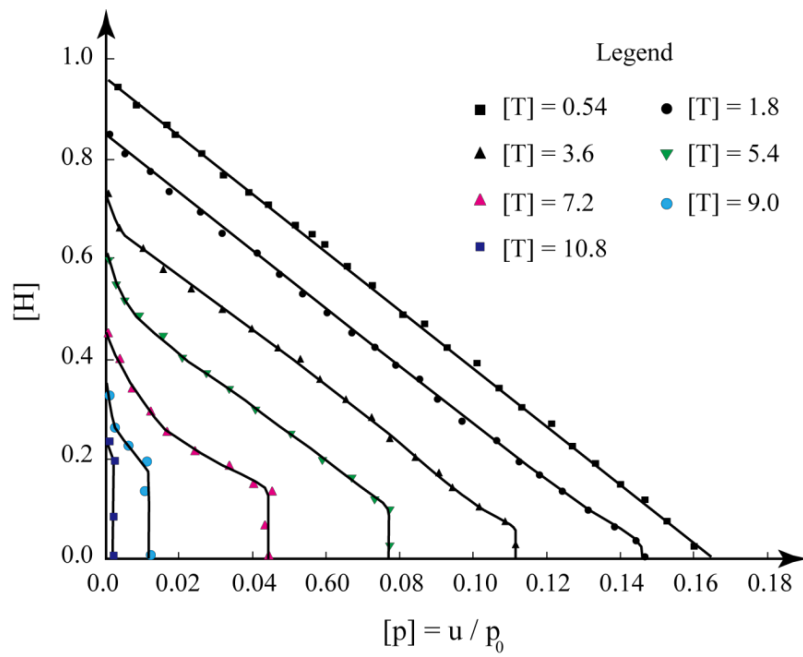
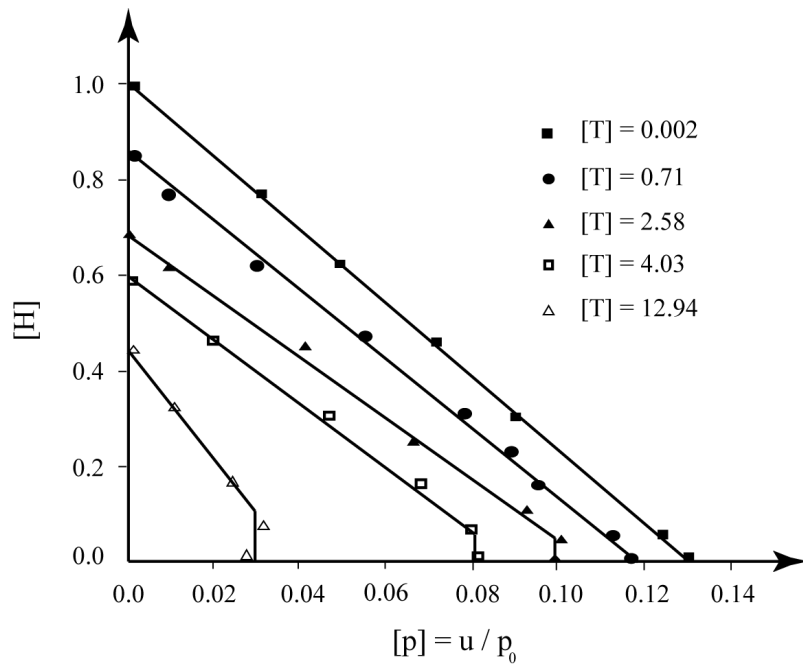


Figure 11. Evolution of excess pore water pressure at the bottom of parallelepiped



(a) Numerical results of the DEM-CFD coupling model



(b) Results from Been [8] (the time is normalized by the characteristic settling time of a particle with diameter being equal to $5 \mu\text{m}$)

Figure 12. Isochrones of excess pore water pressure along the parallelepiped at different times

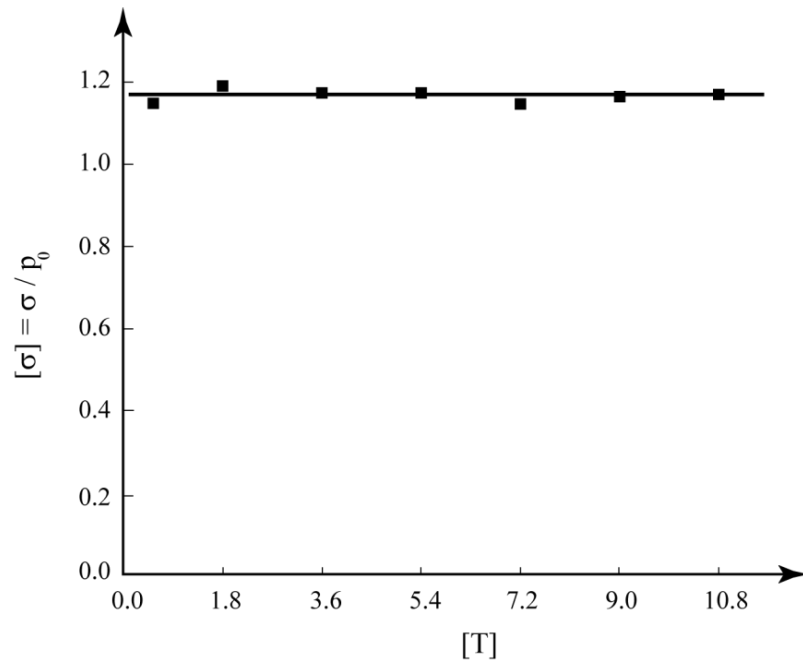


Figure 13. Total stress at the bottom of the parallelepiped

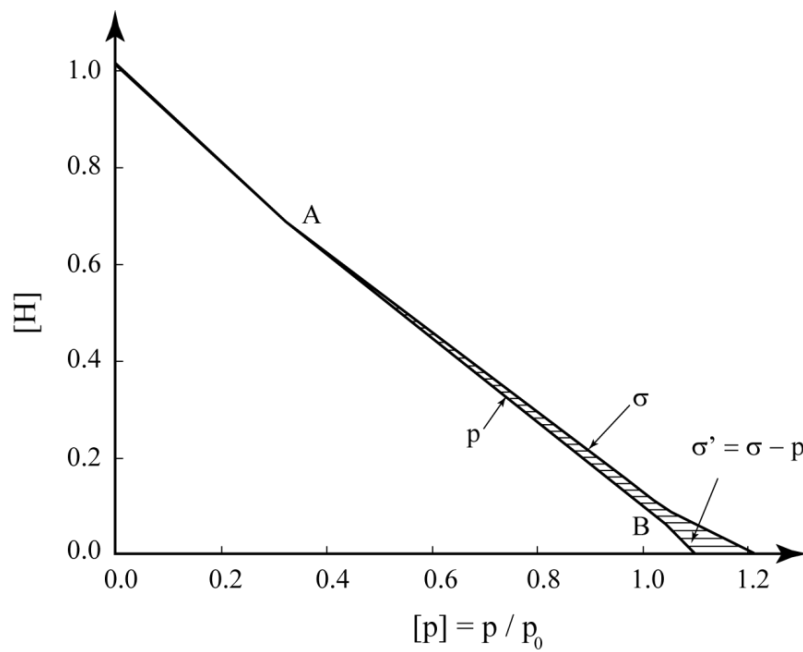


Figure 14. Distribution of total stress and pore water pressure along the parallelepiped at $[T] = 3.6$

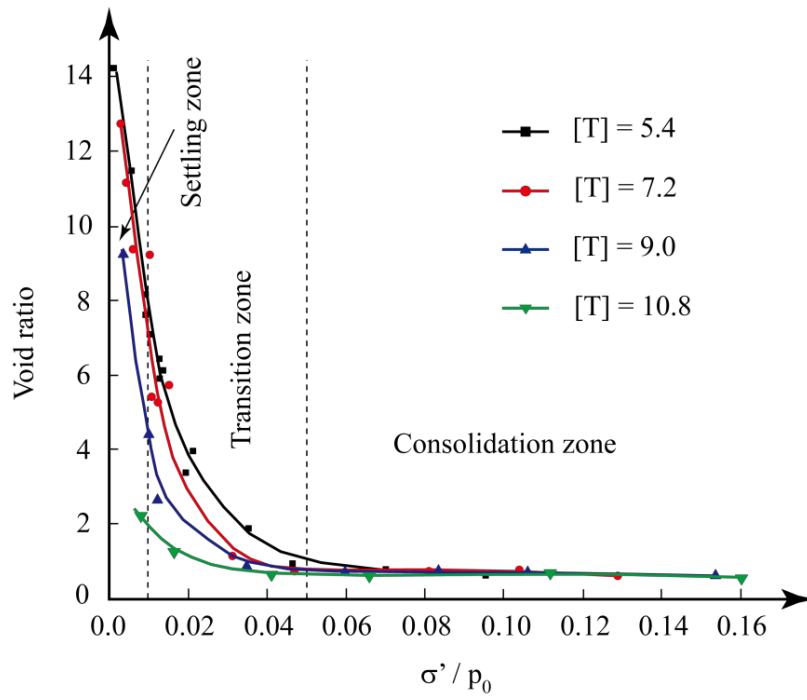


Figure 15. Relationship between the void ratio and normalized effective stress at various simulation times

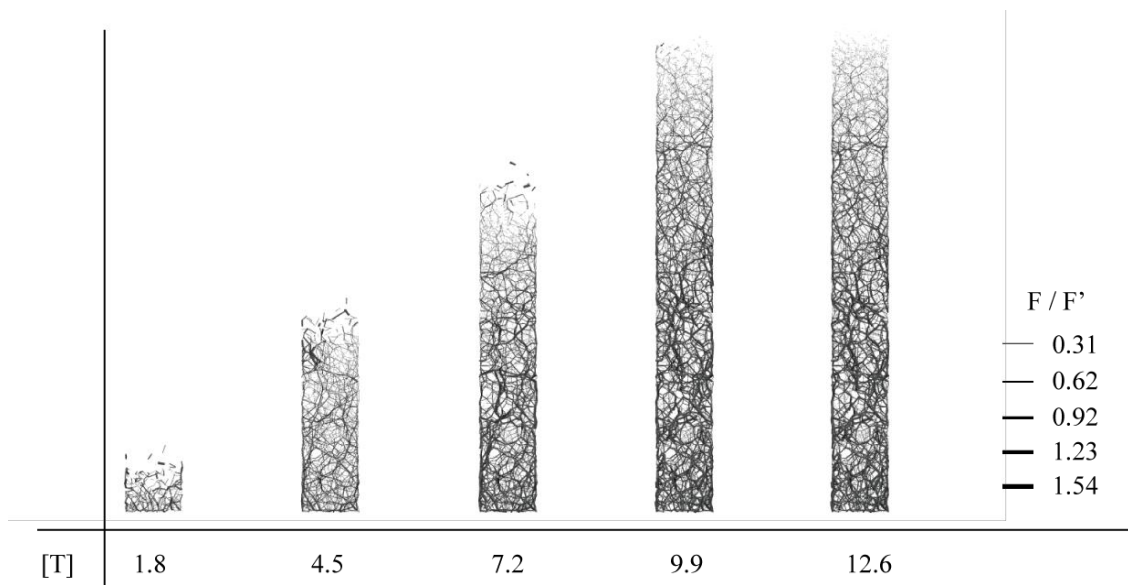


Figure 16. Force chains of the sediments at different simulation times

Table 1. Some correlations of drag force coefficient for spherical particles

Stokes [42]	$\frac{24}{Re}$
Newton (Inertial) [3]	0.44
Schiller and Naumann [50]	$\begin{cases} \frac{24}{Re}(1.0 + 0.15 Re^{0.687}) & Re \leq 1000 \\ 0.44 & Re > 1000 \end{cases}$
DallaValle [46]	$\left[0.63 + \frac{4.8}{\sqrt{Re}}\right]^2$
Brown and Lawler [47]	$\frac{24}{Re}(1 + 0.150 Re^{0.681}) + \frac{0.407}{1 + \frac{8710}{Re}}$

Table 2. Input parameters of the simulations for granular sedimentation

DEM Parameters	Value	CFD Parameters	Value
Particle diameter, d (mm)	[1.8, 3.8]	Fluid density, ρ_f (kg/m ³)	1000
Granular density, ρ_s (kg/m ³)	2650	Viscosity, μ (Pa·s)	0.001
Normal stiffness, K_n (N/m)	3.0×10^7		
Shear stiffness, K_s (N/m)	2.7×10^7	Simulation Parameters	Value
Particle friction angle, ϕ_μ (°)	30	Gravity, g (m/s ²)	-9.81
Coefficient of rolling stiffness, β	1.0	DEM Time step size, Δt_s (s)	10^{-7}
Coefficient of plastic moment, η	0.1	CFD Time step size, Δt_f (s)	10^{-5}
		Coupling frequency*, α	100

* The coupling frequency is the number of iteration steps used in the DEM in one coupling interval.

Electronic Supplementary Material

[Click here to download Electronic Supplementary Material: particles settling in 3D\(animation starts after 5 seconds\).gif](#)

Electronic Supplementary Material

[Click here to download Electronic Supplementary Material: single particle settling - velocity contour.gif](#)

Electronic Supplementary Material

[Click here to download Electronic Supplementary Material: single particle settling - velocity vectors.gif](#)